Shapes of rotating normal fluid ³He versus superfluid ⁴He droplets in molecular beams

Deepak Verma¹, Sean M. O. O'Connell¹, Alexandra J. Feinberg¹, Swetha Erukala¹, Rico M. Tanyag^{1,2}, Charles Bernando^{3,4}, Weiwu Pang⁵, Catherine A. Saladrigas^{6,7}, Benjamin W. Toulson⁶, Mario Borgwardt⁶, Niranjan Shivaram^{8,9}, Ming-Fu Lin⁸, Andre Al Haddad¹⁰, Wolfgang Jäger¹¹, Christoph Bostedt^{10,12}, Peter Walter⁸, Oliver Gessner^{6*} and Andrey F. Vilesov^{1,3*}

¹Department of Chemistry, University of Southern California, Los Angeles, California 90089, USA

²Institute for Optics and Atomic Physics, Technical University of Berlin, Berlin 10623, Germany

³Department of Physics and Astronomy, University of Southern California, Los Angeles, California 90089, USA

⁴School of Information Systems, BINUS University, Jalan K.H. Syahdan No. 9, Kemanggisan, Palmerah, Jakarta

11480 Indonesia

⁵Viterbi School of Engineering, University of Southern California, Los Angeles, California 90089, USA
 ⁶Chemical Sciences Division, Lawrence Berkeley National Laboratory, Berkeley, California 94720, USA
 ⁷Department of Chemistry, University of California, Berkeley, California 94720, USA
 ⁸LCLS, SLAC National Accelerator Laboratory, 2575 Sand Hill Road, Menlo Park, California 94025, USA
 ⁹Department of Physics and Astronomy, Purdue University, West Lafayette, Indiana 47907, USA
 ¹⁰Laboratory for Femotochemistry (LSF), Paul Scherrer Institute, Forschungsstrasse 111, 5232 Villigen-PSI, Switzerland

¹¹Department of Chemistry, University of Alberta, Edmonton, Alberta T6G 2G2, Canada
 ¹²LUXS Laboratory for Ultrafast X-ray Sciences, Institute of Chemical Sciences and Engineering, École Polytechnique Fédérale de Lausanne (EPFL), CH-1015, Lausanne, Switzerland

*Authors to whom correspondence should be addressed. Electronic addresses: ogessner@lbl.gov; and <u>vilesov@usc.edu</u>.

May 28st, 2020

Abstract

Previous single-pulse extreme ultraviolet and X-ray coherent diffraction studies revealed that superfluid ⁴He droplets obtained in a free jet expansion acquire sizable angular momentum, resulting in significant centrifugal distortion. Similar experiments with normal fluid ³He droplets may help elucidate the origin of the large degree of rotational excitation and highlight similarities and differences of dynamics in normal and superfluid droplets. Here, we present the first comparison of the shapes of isolated ³He and ⁴He droplets following expansion of the corresponding fluids in vacuum at temperatures as low as ~ 2 K. Large 3 He and 4 He droplets with average radii of ~160 nm and ~350 nm, respectively, were produced. We find that the majority of the shapes of ³He droplets in the beam correspond to rotating oblate spheroids, in agreement with previous observations for ⁴He droplets. The aspect ratio of the droplets is related to the degree of their rotational excitation, which is discussed in terms of reduced angular momenta (Λ) and reduced angular velocities (Ω) , the average values of which are found to be similar in both isotopes. This similarity suggests that comparable mechanisms induce rotation regardless of the isotope. We hypothesize that the observed distribution of droplet sizes and angular momenta originate from processes in the dense region close to the nozzle, where a significant velocity spread and frequent collisions between droplets induces excessive rotation followed by droplet fission.

1. Introduction

Bosonic superfluid helium-4 (4He) droplets, produced in molecular beams, constitute a versatile medium for experiments in physics and chemistry. Notably, droplets consisting of a few thousand He atoms are frequently used as ultra-cold matrices for the spectroscopic interrogation of single molecules, radicals, ionic species, and diverse clusters [1-6]. Single molecules embedded in ⁴He droplets can also provide a unique probe for superfluidity on atomic-length scales via renormalization of molecular rotational constants [7-9]. More recently, experiments have been extended to much larger ⁴He droplets, containing up to ~10¹¹ atoms, and ranging in diameter from hundreds of nanometers up to a few micrometers [10]. Single droplets in this size range have been studied by ultrafast coherent scattering using femtosecond X-ray and XUV pulses from free electron lasers (FEL) and intense, laboratory-based high-order harmonic sources [11-17]. It was found that large ⁴He droplets can have sizable angular momentum and can be subject to considerable centrifugal distortion [11,14-17]. Rotation of superfluid ⁴He droplets is associated with the creation of quantum vortices, a physical manifestation of quantized angular momentum in the bosonic species [18-21]. Quantum vortices inside ⁴He droplets have been visualized by doping them with a large number of xenon (Xe) atoms. The dopants are attracted to the vortices, inducing aggregation around the vortex cores and the formation of filament-shaped clusters [11-13,17].

Experiments involving droplets of the rare fermionic helium-3 isotope (3 He) have also been performed [7,22-30]. While 3 He may exist as a superfluid under temperatures T \approx 1 mK [31,32], it is a normal fluid at typical molecular beam temperatures of \sim 0.15 K [29]. Recent density functional calculations show that the rotating 3 He droplets should follow corresponding classical shapes [33]. It is important to expand X-ray imaging experiments to rotating 3 He droplets to enable a direct comparison of droplet shapes and rotational properties of the two quantum fluids.

In this article, we report on the characterization of ³He droplets produced with nozzle temperatures as low as ~2 K. Using ultrafast X-ray scattering at an XFEL, the properties of individual, free ³He and ⁴He droplets are analyzed and their size, shape and angular momenta are compared. A wide range of ³He and ⁴He droplet sizes are obtained with average radii of 162 nm and 355 nm, respectively. An overwhelming majority of the droplets have pseudo-spheroidal shapes, characterized by the aspect ratio of the major and minor axes. From the aspect ratio, the reduced angular momenta and angular velocities are obtained, using the corresponding stability

diagram for classical viscous droplets [14,34,35]. The aspect ratios of droplets from both isotopes are found to have average values of 1.074 for ³He and 1.088 for ⁴He. Accordingly, the reduced angular momentum and reduced angular velocity in ³He and ⁴He droplets are similar. Comparison of the results obtained with ⁴He and ³He at different expansion conditions may help to gain a better understanding of the mechanism underlying the production of rotating droplets in free nozzle beam expansion sources.

2. Experimental

He droplets are produced by expanding pressurized He through a cryogenic nozzle with a 5 μm orifice into vacuum, the details of which are described elsewhere [1,4,5,10]. In vacuum, the temperature of the droplets further decreases via evaporative cooling down to 0.15 K and 0.38 K for ³He [29] and ⁴He [7], respectively. Phase diagrams for ³He and ⁴He containing some typical expansion isentropes are presented in Section S1 of the Supplementary Material (SM) [36] (see also references [37-39] therein). Considering the lower critical point of ${}^{3}\text{He}$ ($T_{C} = 3.3 \text{ K}, P_{C} = 1.1$ atm) compared to that of ${}^{4}\text{He}$ (T_C = 5.2 K, P_C = 2.3 atm), lower nozzle temperatures are required to obtain ³He droplets of the same sizes as those consisting of ⁴He. For example, for a nozzle stagnation pressure of $P_0 = 20$ bar, previous experiments demonstrate that ⁴He droplets with an average number of atoms $\langle N_4 \rangle = 10^7$ are produced at a nozzle temperature of $T_0 = 7$ K, [10] while $T_0 = 5$ K is required to obtain ³He droplets with the same average number of atoms $\langle N_3 \rangle = 10^7$ [25-27,40]. The temperature difference of 2 K in T₀ correlates well with the corresponding difference in critical temperatures of the two isotopes. Large ⁴He droplets can be produced with modern closed-cycle refrigerators that can reach temperatures down to ~3.5 K. However, to reach the lower temperatures required to produce large ³He droplets, we instead employed a liquid helium flow cryostat, the LT3 from Advanced Research Systems, with a cooling power of up to 1 W at 1.8 K. Droplets of 3 He and 4 He are produced at constant $P_{0} = 20$ bar and varying T_{0} , ranging from 2 to 4.5 K. The temperature was measured using a calibrated silicon diode (Lakeshore DT-670-CU) attached to the copper block close to the nozzle.

Due to the considerable cost of 3 He gas, a recycling system is employed during the experiments as described in Section S2 of the SM [36] (see also references [41,42] therein). Filling the system requires about 10 L·bar of room temperature 3 He. For comparison, at standard operating conditions ($T_0 = 3 \text{ K}$, $P_0 = 20 \text{ bar}$), the flow rate of the He gas is $\sim 3 \text{ cm}^3 \cdot \text{bar/s}$ and the filling amount of gas

would only be sufficient for about 1 hour of operation. During the experiments, ³He gas is continuously collected from the exhausts of the backing scroll pumps, purified in a liquid nitrogen cooled zeolite trap, pressurized by a metal membrane compressor and resupplied to the nozzle with minimal losses. Any contaminants are constantly removed from the ³He sample by the recycling system. The droplet source was stable over several days, indicating the purity of the ³He remained high throughout the experiment. The ³He gas used is 99.9% pure with the remaining 0.1% impurity being mostly ⁴He. The residual ⁴He will be mostly dissolved in the ³He droplets, taking into account that its solubility is ~0.1% at 0.15K [32]. Any possible pockets of ⁴He rich phase in ³He droplets are too small to give rise to any measurable effects in the diffraction patterns. Based on the rest gas pressure of less than 10⁻⁷ mbar and a beam path length from the nozzle to the interaction point of about 70 cm, the droplets will capture, on average, fewer than 500 rest gas particles (mostly water molecules), again too small a number to be detected in the diffraction experiments.

The experiments are performed using the LAMP end station at the Atomic, Molecular and Optical (AMO) instrument of the Linac Coherent Light Source (LCLS) XFEL [43,44]. The focused XFEL beam (~2 μ m full-width-at-half-maximum, FWHM) intersects the He droplet beam ~70 cm downstream from the nozzle. The XFEL is operated at 120 Hz, a photon energy of 1.5 keV (λ = 0.826 nm), a pulse energy of ~1.5 mJ and a pulse duration of ~100 fs (FWHM). The small pulse length and large number of photons per pulse (~10¹²) enables the instantaneous capture of the shapes of individual droplets. Diffraction images are recorded with a pn-charge-coupled device (pnCCD) detector containing 1024×1024 pixels, each 75×75 μ m² in size, which is centered along the XFEL beam axis ~735 mm downstream from the interaction point. The detector consists of two separate panels (1024×512 pixels each), located closely above and below the X-ray beam. Both panels also have a central, rectangular section cut-out to accommodate the primary X-ray beam. The diffraction patterns are recorded at small scattering angles and, thus, predominantly contain information on the column density of the droplets in the direction perpendicular to the detector plane.

3. Results

Figure 1 shows several diffraction patterns from pure ³He droplets. The images are characterized by sets of concentric contours. Images in Figures 1(a) and (b) exhibit a series of circular and elliptical contours, respectively, with different spacing between their respective rings.

Figure 1(c), however, shows an elongated diffraction contour with pronounced streaks radiating away from the center. These diffraction patterns are characteristic of spherical (Figure 1(a)), and spheroidal (oblate) or capsule (prolate) (Figure 1(b) and(c)) droplet shapes, as previously observed in ⁴He droplets [11,14,16,17]. Spheroidal and prolate shapes result from centrifugal deformation of droplets with considerable angular momentum.

The droplet shapes are characterized by the distances between the center and the surface in three mutually perpendicular directions: $a \ge b \ge c$. For an oblate axisymmetric droplet, a = b > c, with c along the rotation axis, whereas a > b > c in the case of triaxial prolate shapes with c along the rotation axis [11,14]. The observed diffraction patterns do not provide direct access to the actual values of a, b and c, due to the droplets' unknown orientations with respect to the X-ray beam. Instead, the images are characterized by the two half-axes of the projection of a droplet onto the detector plane, which will be referred to as A and C (A > C), corresponding to a projection aspect ratio, AR = A / C. For an axisymmetric oblate droplet having an unknown orientation with respect to the X-ray beam, the value of A corresponds to the a-axis, whereas the value of C only constitutes an upper bound for the C-axis. In the case of a triaxial droplet, the value of C gives a lower bound for the C-axis and an upper bound for the C-axis. In this section, we will discuss the experimental results in terms of the apparent C and C and C and C are obtained from the diffraction patterns as described elsewhere (SM in Reference [14]).

The values of the half axes A and C, as well as their ARs, are noted for each panel in Figure 1. The calculated A and C values from Figure 1(a) are very similar (within \sim 3%), indicative of a spherical droplet shape or a spheroid with its symmetry axis aligned perpendicular to the detector plane. The diffraction pattern shown in Figure 1(b) originates from a droplet with larger values of A and C. Here, the two half-axes differ by \sim 34% (AR = 1.34), which is indicative of a spheroidal or ellipsoidal droplet. The streaked diffraction image in Figure 1(c) corresponds to a strongly deformed, capsule-shaped droplet with AR = 1.95. The capsule shape is indicated by the small curvature of the streak, as discussed earlier [14,16]. All images in Figure 1 exhibit blank horizontal stripes along their middle sections. These result from the gap between the upper and the lower panels of the pnCCD detector. Vertical stripes on the lower panel are caused by imperfect data readout for strong diffraction images.

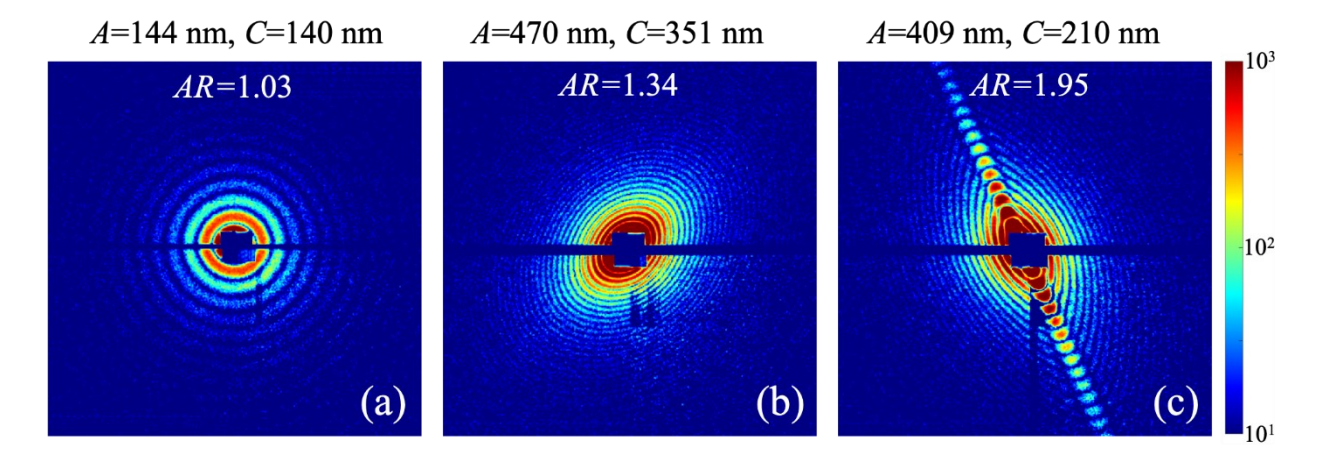


Figure 1. Diffraction patterns of pure 3 He droplets shown on a logarithmic color scale as indicated on the right. Images represent the central 660×660 detector pixels. Corresponding droplet projection half-axes (A, C) and their aspect ratio (AR) are displayed at the top of each image.

During the measurements, approximately 900 intense diffraction images from pure ³He droplets are obtained, each providing a unique set of A and C values. Similar measurements are performed for ⁴He droplets, providing ~300 patterns as an independent reference for comparison. The measurements for a given isotopic fluid do not exhibit any systematic variation with nozzle temperature, thus, the results obtained at different temperatures are combined to improve statistics. Table S1 in the SM [36] lists the nozzle temperatures and corresponding numbers of recorded diffraction images for all experimental runs. Figure 2(a) displays the measured distribution of the droplet's major half axis, A, for ³He and ⁴He droplets, as represented by blue and red bars, respectively. The average value of A of ⁴He droplets is approximately a factor of two larger than that of 3 He droplets. The values for the 3 He droplets vary between A=52 nm and A=796 nm, whereas 4 He droplets exhibit a larger spread, ranging from A=55 nm to A=1250 nm. Figure 2(b) shows the AR distribution for ³He and ⁴He droplets. The largest ARs are 1.99 for ³He and 1.72 for ⁴He. Figures 2(a) and (b) show that both the values of A and (AR-1) follow exponential distributions. Panel (c) in Figure 2 shows the average aspect ratio for each of the bins in panel (a) for droplets with AR < 1.4, which correspond to oblate pseudo-spheroidal shapes as discussed in the following. The results of single measurements with AR > 1.4 in panel (c) are shown by stars. It is seen that in ³He droplets, the average aspect ratio increases linearly from ~1.03 in small droplets with A < 100 nm to ~1.15 in larger droplets with $A \sim 600$ nm. Corresponding points for 4 He droplets also follow linear dependence with a somewhat smaller slope and have $<\!AR\!> \sim 1.12$ at A > 600 nm. The AR distribution in each bin from Figure 2(a) is found to be close to exponential. In contrast to the temperature-independent droplet sizes reported here, previous measurements on 4 He droplets found continuous increases in sizes with decreasing temperature [10]. At $T_0 < 4$ K and $P_0 = 20$ bar, 4 He expansion leads to the formation of a jet that breaks up into micron-sized droplets due to Rayleigh instability [10,45,46]. This mechanism gives rise to an extremely collimated beam of droplets, the occurrence of which was not observed during this work with either 3 He or 4 He. We conclude that, most likely, the flow through the nozzle in this work was affected by imperfections such as microscopic damage or partial obstruction by some solid impurities. Previous experiments with 4 He droplets in our group demonstrated that, under such conditions, decreasing the nozzle temperature below a certain value does not result in any increase in average droplet size [47], which is in agreement with the observations in this work.

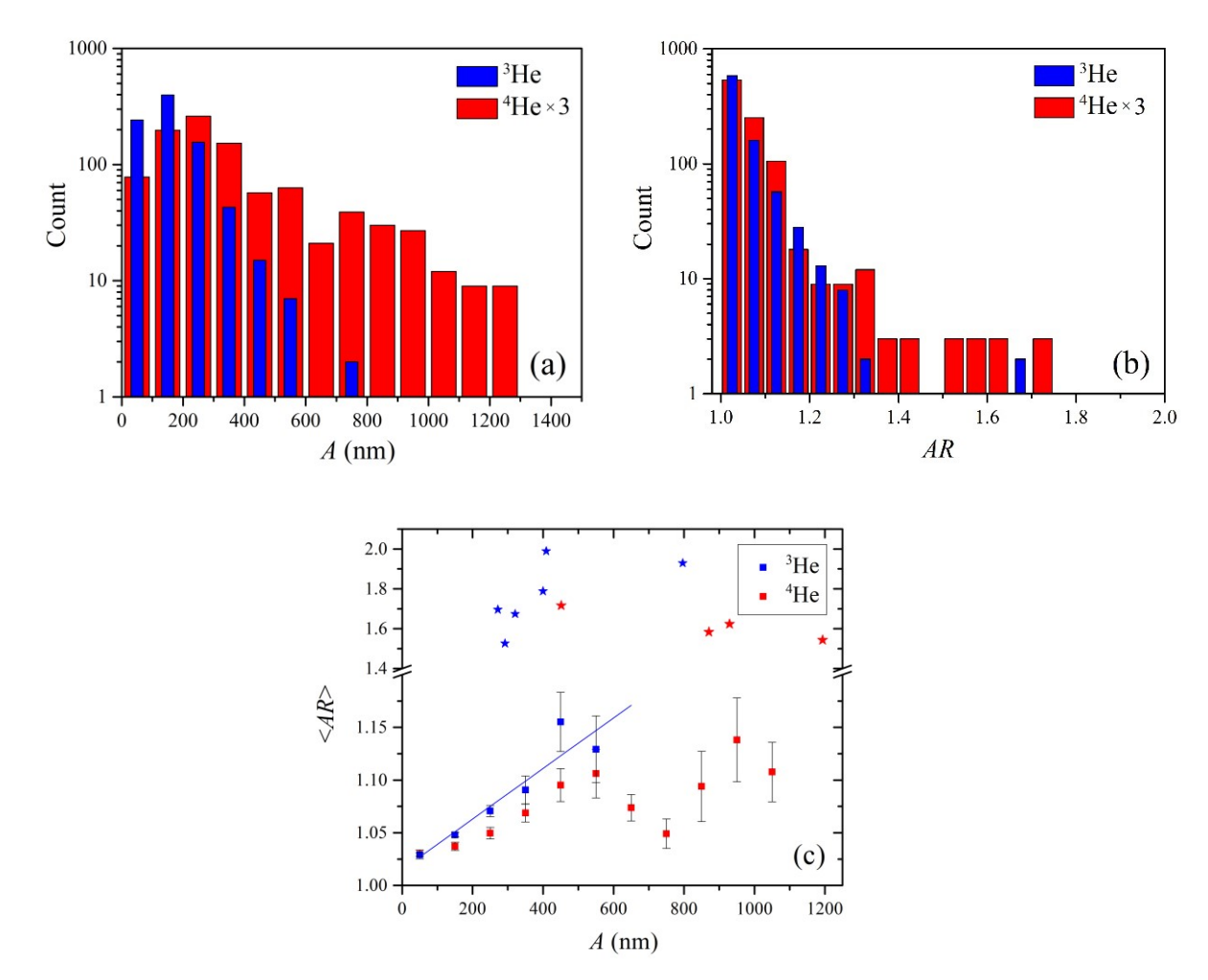


Figure 2. Droplet size (a) and aspect ratio (b) distributions for 3 He (blue) and 4 He (red) isotopes presented in logarithmic scales. The counts for 4 He were multiplied by a factor of 3 for the ease of comparison, as the total number of diffraction images obtained for 3 He and 4 He were \sim 900 and \sim 300, respectively (see Table S1 in SM). Squares in panel (c) show average AR as obtained for each bin in panel (a) for the points with AR < 1.4. The results of single measurements with AR > 1.4 in panel (c) are shown by stars. The blue line in panel (c) represents a linear fit of the data points (blue squares) for 3 He droplets.

4. Discussion

4.1. Droplet size distribution

From Figure 2(a), we notice that the observed droplet size distributions peak at some small value of A, decrease sharply towards smaller A, and decrease more gradually towards larger A. The measured distribution reflects the actual distribution in the beam multiplied by the detection efficiency for a droplet of apparent half-axis A in the diffraction experiment. In the SM [36], it is shown that for a spherical droplet, the detection efficiency scales as $ln \frac{R^4}{R_0^4}$ for $R \ge R_0$ and it is zero for $R < R_0$, where R is the radius of the droplet and $R_0 \approx 50$ nm is the radius of the smallest detectable droplet. Accordingly, for $R >> R_0$ the detection probability is a slowly changing logarithmic function of R. However, as R approaches R_0 , the detection efficiency goes to zero, which explains the decrease of the counts at small A in Figure 2(a). In view of the approximate nature of the derivation, no corrections regarding the detection efficiency were applied in this work.

Droplet size distributions are usually discussed in terms of the number of atoms per droplet, owing to the detection technique, which is often based on mass spectroscopy [48]. For an oblate droplet the number of He atoms is given by $N = \frac{4\pi na^2c}{3}$, where n is the number density of liquid 3 He or 4 He at low temperature, with values of 1.62×10^{28} m⁻³ [32] and 2.18×10^{28} m⁻³ [49], respectively. Here, we approximate the true values of a and c for each droplet by the measured projection values of A = a and $C \le c$. Since, as discussed in the following section, the average aspect ratio of the droplets is close to unity, this approximation will overestimate the droplet number sizes by a few percent, which is comparable to the statistical error. Accordingly, average number sizes for droplets with aspect ratios of less than 1.4 are $< N_3 > = (5.6 \pm 0.1) \times 10^8$ and $< N_4 > = (5.6 \pm 0.1) \times 10^8$ = $(1.1 \pm 0.1) \times 10^{10}$. Figure 3 shows the number size distribution for ³He droplets on a natural logarithmic scale. For comparison, the red line indicates an exponential distribution $P(N_3)$ $\frac{S}{\langle N_2 \rangle} \exp\left(-\frac{N_3}{\langle N_2 \rangle}\right)$, with S being the total number of detected droplets. This approximation is in good agreement with the experimental data for sizes $N_3 \le 3 \times 10^9$. An exponentially declining size distribution was also found in a recent study of ⁴He droplets obtained from a pulsed nozzle at the FERMI FEL [16]. In comparison, the size distribution of smaller 3 He droplets with $N_{3} \le 10^{7}$ obtained at $P_0 = 20$ bar and $T_0 \ge 5$ K was found to be close to log-normal [40].

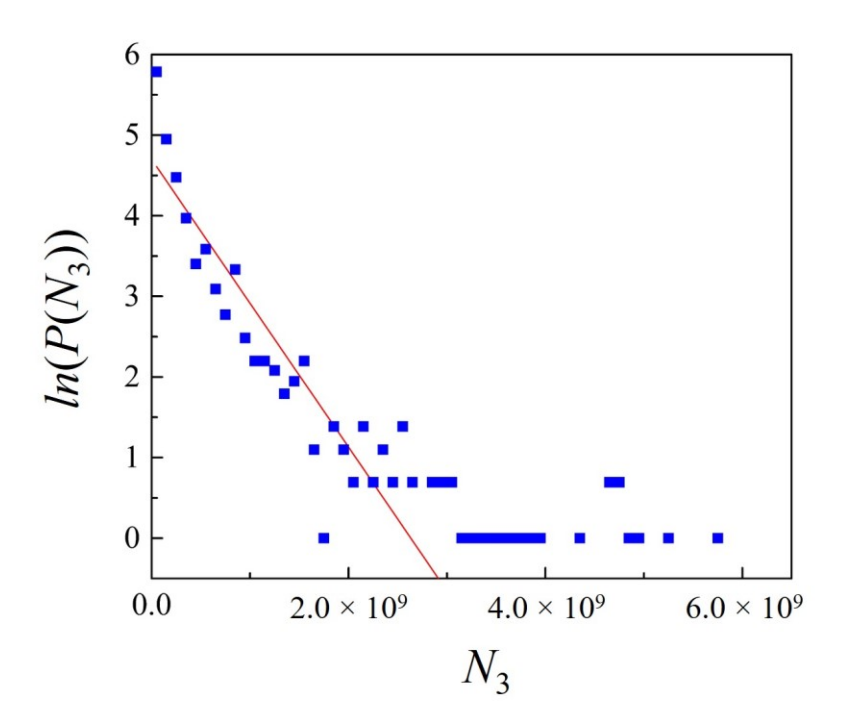


Figure 3. Measured size distribution of 3 He droplets (blue squares). The red line represents $\ln(P) = 4.7 - N_3 / < N_3 >$ (blue squares) with $< N_3 > = 5.6 \times 10^8$, see the text for details. The figure does not show 9 droplets in the range $N_3 = 7 \times 10^9 - 2 \times 10^{10}$, which are off scale.

4.2. Droplet aspect ratios

The aspect ratios provide access to the angular momentum and angular velocity of the droplets. One can obtain the average actual aspect ratio $\langle ar \rangle$ from the average apparent aspect ratio $\langle AR \rangle$ assuming a random droplet orientation as described in the following.

In classical droplets, the largest aspect ratio of stable, axially symmetric droplets is ar = 1.47 [34,35]. About 99% of the measurements in Figure 2 have AR < 1.4, in agreement with previous measurements in ⁴He droplets [11,14-16]. Here, we assume that an overwhelming majority of droplets with AR < 1.4 have oblate, axially symmetric shapes. We also assume that the data set contains less than ~ 10 events from prolate He droplets that are oriented in such a way that their projections yield AR < 1.4 and cannot be distinguished from oblate droplets. This estimate is

based on the number of events producing AR > 1.4, which are entirely ascribed to prolate droplets. For more details, see Fig. 11 and the corresponding text in Ref. [14]. For shapes with AR < 1.4, the average values for the observed major half axis A and aspect ratio AR are $<A_3>=160 \pm 3$ nm, $<AR_3>=1.049 \pm 0.003$, $<A_4>=348 \pm 14$ nm, $<AR_4>=1.059 \pm 0.005$, where the subscripts 3 and 4 refer to 3 He and 4 He, respectively.

To translate the measured $\langle AR \rangle$ into the actual $\langle ar \rangle$, we assume a spheroid with a well-defined ar and calculate its projection on the detector plane when its symmetry axis c forms an angle α with the normal to the plane. The aspect ratios of the diffraction pattern (AR) and of the spheroid off which the X-rays diffract (ar) are related by: $AR = \sqrt{\cos^2(\alpha) + ar^2 \sin^2(\alpha)}$ (see Eq. (S2.8) in the SM to [11]). The average AR of an ensemble of randomly aligned droplets is then calculated as $\langle AR \rangle = \int_0^{\frac{\pi}{2}} AR(\alpha) \cdot \sin(\alpha) \cdot d\alpha$, where $\sin(\alpha)$ represents the probability of finding a spheroid at angle α . Integration and second-order expansion near $\langle AR \rangle = 1$ yields $\langle AR \rangle - 1 = \frac{2}{3}(ar-1) + \frac{1}{15}(ar-1)^2$. The expression is approximately linear within less than 5% error in the range of $1 \le ar \le 1.4$. Due to the linear relationship between $\langle AR \rangle$ and ar, the same formula also applies when considering not just an orientation-averaged ensemble with one specific ar, but also averages over all orientations, thus $\langle ar \rangle - 1 \approx \frac{3}{2}(\langle AR \rangle - 1)$. From this relationship, the average true aspect ratios for 3 He and 4 He droplets are derived as $\langle ar \rangle_3 = 1.074 \pm 0.005$ and $\langle ar \rangle_4 = 1.088 \pm 0.008$, respectively.

4.3. Average angular momenta and angular velocities of ³He and ⁴He droplets

As previously described for ⁴He droplets [11,14-17], we ascribe the shape deformation in ³He droplets to centrifugal distortion. It has been reported that the shapes of rotating ⁴He droplets closely follow the equilibrium shapes of classical droplets having the same values of angular momentum [14,16,17,20,21]. This pattern is also expected to be the case of ³He droplets, which at the temperature of these experiments (~0.15 K) [29] should behave classically due to the high viscosity of about 200 μP and small mean free path (a few nm) of elementary excitations at this temperature [32]. In recent density functional calculations, the shapes of rotating ³He droplets were found to be very close to those predicted for classical droplets [33]. The blue curves in Figure 4

show the stability diagram of the classical droplets in terms of the reduced angular momentum (Λ) and reduced angular velocity (Ω), which are given by [34,35],

$$\Lambda = \frac{L}{\sqrt{8\sigma\rho R^7}} \tag{1}$$

$$\Omega = \sqrt{\frac{\rho R^3}{8\sigma}} \cdot \omega \tag{2}.$$

Here, L and ω are the angular momentum and angular velocity, respectively, σ is the surface tension of the liquid, ρ is the liquid mass density, and R is the droplet radius in a quiescent state. For liquid ⁴He and ³He at low temperature, the surface tensions are $\sigma_4 = 3.54 \times 10^{-4}$ N/m [49] and $\sigma_3 = 1.55 \times 10^{-4}$ N/m [50], respectively, while their densities are $\rho_4 = 145$ kg/m³ [49] and $\rho_3 = 82$ kg/m³ [32]. With increasing Λ , the droplet's equilibrium shape transitions from spherical to oblate axially symmetric, which is shown by the solid blue curve. At $\Omega \approx 0.56$, $\Lambda \approx 1.2$, $ar \approx 1.47$, the stability curve bifurcates into two branches; an unstable upper branch (dashed blue curve) representing axially symmetric droplets and a stable lower branch (dotted blue curve) representing prolate triaxial droplets. The stable prolate branch represents triaxial ellipsoidal and capsule shaped droplets with 1.2 < Λ < 1.6, and dumbbell-shaped droplets at Λ > 1.6 [14,16,34,35]. For Λ > 2, droplets become unstable and break up. Also shown in Figure 4 is the ar of droplets along the axisymmetric branch as a function of Λ , which is represented by the red curve [14]. Using an exponential distribution of the ar values: $P(ar-1) = \frac{1}{\langle ar-1 \rangle} \exp\left(-\frac{ar-1}{\langle ar-1 \rangle}\right)$, and the functions of $\Lambda(ar)$ and $\Omega(ar)$ in Figure 4, integration over ar gives the average Λ and Ω for ³He and ⁴He droplets to be $<\Lambda_3>=0.47$, $<\Omega_3>=0.27$ and $<\Lambda_4>=0.51$, $<\Omega_4>=0.29$. Those values are indicated in Figure 4 as green circles and black crosses, respectively. Very similar values were obtained for ³He by integrating a double exponential distribution of the form:

 $P(ar-1,A) = \frac{1}{\langle ar(A)-1\rangle} \exp\left(-\frac{ar-1}{\langle ar(A)-1\rangle}\right) \frac{1}{\langle A\rangle} \exp\left(-\frac{A}{\langle A\rangle}\right)$ where the values of ar(A) were obtained from the blue line in Figure 2(c) multiplied by 1.5. Although the values of $\langle AR\rangle$ vs A in Figure 2(c) lay somewhat lower for ⁴He than for ³He, the corresponding average values for ⁴He are larger due to larger prevalence of large ⁴He droplets. From the values of $\langle \Lambda_{3,4} \rangle$ and $\langle \Omega_{3,4} \rangle$ and using equations (1, 2), the angular momentum (L) is obtained as $L_3 = 1.5 \times 10^9 \, \hbar$ and $L_4 = 6.9 \times 10^{10} \, \hbar$ for the average-sized ³He and ⁴He droplets, respectively. Next, L per atom of the droplet is

obtained as 5.7 \hbar and 19.3 \hbar for ³He and ⁴He droplets, respectively. Lastly, ω was calculated as 1.6×10^7 rad/s and 5.9×10^6 rad/s for ³He and ⁴He, respectively. Although the ⁴He droplets and ³He droplets have similar $<\Lambda>$, ⁴He droplets have about a factor of three larger L per atom. Mathematically, this effect stems from the different factors of $\sqrt{\sigma\rho R^7}$ in Equation (1) in ³He and ⁴He droplets.

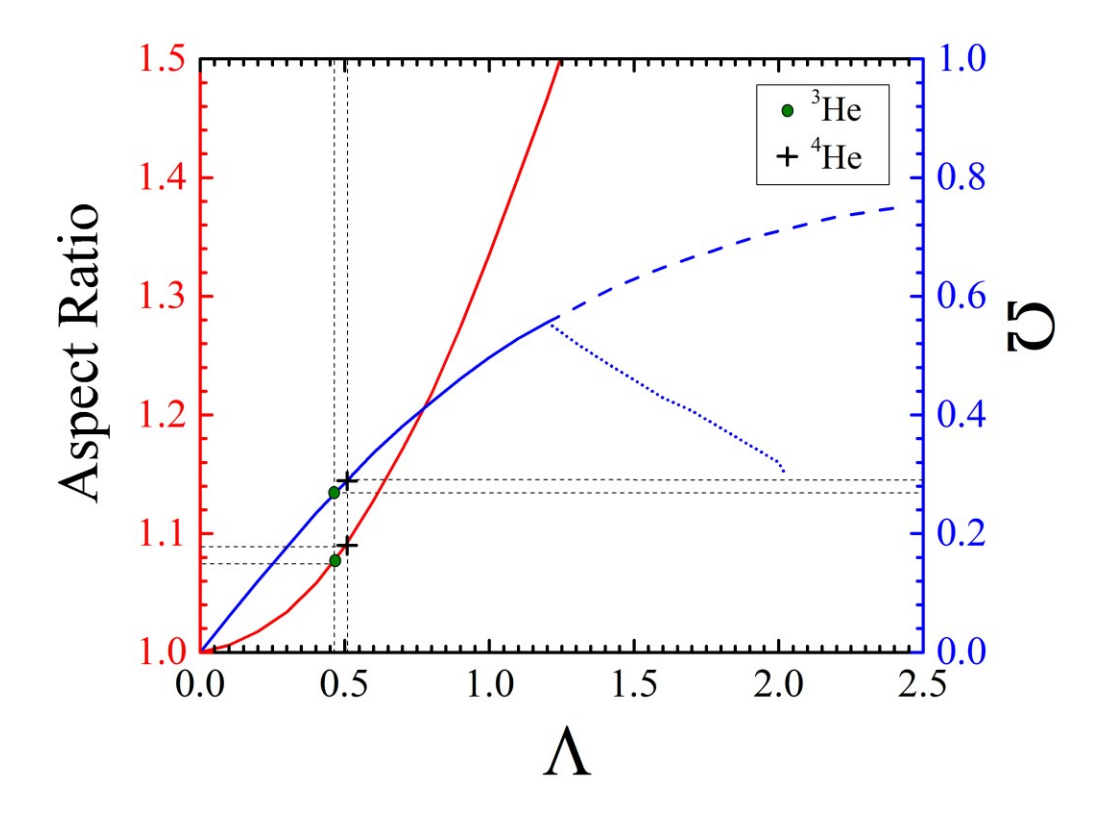


Figure 4. Red curve: Calculated aspect ratio as a function of reduced angular momentum (Λ) for axially symmetric oblate droplet shapes. Blue curve: stability diagram of rotating droplets in terms of reduced angular velocity (Ω) and reduced angular momentum (Λ). The upper branch (dashed blue) corresponds to unstable axially symmetric shapes. The lower branch (dotted blue) is associated with prolate triaxial droplet shapes resembling capsules and dumbbells. The green circle and black cross on the red curve represent the average $\langle ar \rangle$ for 3 He and 4 He droplets, respectively, obtained in this work (with AR < 1.4). Similar markers on the blue curve indicate the (Ω , Λ) values corresponding to 3 He and 4 He droplets.

4.4. Formation of rotating droplets in the fluid jet expansion

It is remarkable that despite their very different physical properties, 3 He and 4 He droplets have very similar values of Ω and Λ on average. Previous XFEL experiments with 4 He droplets yielded average aspect ratios, 4 AP>, in the range of 1.06-1.08 at $P_{0}=20$ bar and $T_{0}=4-7$ K, which spans average droplet sizes from 200 nm to 1000 nm in diameter (see Figure 4.11 in Reference [47]). Thus, it is noteworthy that very similar average aspect ratios, and therefore Ω and Λ , were obtained at different T_{0} . Comparable 4 AP> were obtained in experiments involving different nozzle plates, including measurements with partially obstructed and intact nozzles [47]. Hence, it seems that the acquired 4 AP> is largely independent of particular nozzles used in the experiments. Similar results for non-superfluid 3 He and superfluid 4 He droplets indicate that the state of the droplets has a small effect on the resulting average reduced angular momentum.

In previous works [14,51], we conjectured that during the passage of fluid helium through the nozzle, the fluid interacts with the nozzle channel walls and acquires vorticity, which is eventually transferred to the droplets [10]. Accordingly, the estimated average angular velocity of 4 He and 3 He droplets is 3.4×10^{7} rad/s and 4.5×10^{7} rad/s, respectively. Such high angular velocities can only be sustained by rather small droplets.

It is challenging to explain the similarities in reduced angular velocity and angular momentum in 3 He and 4 He droplets based on the stability diagram in Figure 4 and the estimated vorticities. Moreover, the half axis and shape distributions in Figure 2, as observed at high vacuum far downstream (\sim 70 cm) from the nozzle, originate from processes in the high-density region inside or close to the nozzle, where collisions between droplets with the dense He gas must play an important role. For example, for a droplet with a radius of 300 nm, rotating at 10^7 rad/s, the peripheral velocity will be \sim 3 m/s, assuming rigid body rotation. In the regime of extensive jet atomization as in this work, a large spread of droplet velocities up to $\Delta v/v \sim 5\%$ has previously been observed [52]. Thus, with a characteristic droplet velocity on the order of 200 m/s, the droplets may have significant relative collision velocities of \sim 10 m/s, which are sufficient to produce rapidly spinning products. Further downstream, presumably a few mm away from the nozzle, the number density of the gas and droplets decrease, the collision rates decrease, and the angular momenta of individual droplets remain constant further downstream.

Although we are currently unable to provide a quantitative model of the processes close to the nozzle, it is instructive to consider the evolution of a droplet driven at some angular velocity as opposed to free droplets with a constant angular momentum. The corresponding driving force may originate from the aforementioned collisions. The prolate branch on the stability curve of driven droplets is unstable at constant ω [34]. Driven droplets will climb along the axially symmetric branch until they reach the bifurcation point at $\Omega = 0.56$ (Figure 4) at which point they will enter the unstable prolate branch. Here, further elongation of the droplets occurs, culminating in their fission. The stable configurations beyond the fission point correspond to two spherical droplets, each having one half the volume of the parent droplet [34]. On the other hand, scission of dumbbell-shaped droplets will result in strongly deformed fragments. Related theoretical studies of nuclear fission indicate that such fragments contain sizable angular momentum [53,54]. Similar to the parent droplets, daughter droplets will acquire angular momentum via collisions. The fission cycle continues until sufficiently small, stable droplets are formed or the droplets are far away from the nozzle, where the driving force diminishes. Because the occurrence of such a cycle is largely independent of the He isotope, the process should yield very similar values of $\langle AR \rangle$, $\langle \Lambda \rangle$ > and $<\Omega>$, independent of the droplet size and composition. This model is also consistent with the trend apparent in Fig. 2(c) that larger droplets exhibit larger values of $\langle AR \rangle$.

5. Conclusions

In this work, bosonic ⁴He and, for the first time, fermionic ³He droplets are studied by single-pulse X-ray coherent diffractive imaging. Statistics of the droplets' sizes, aspect ratios, reduced angular momenta and reduced angular velocities are compared for superfluid ⁴He droplets and normal fluid ³He droplets. Since the experiments only give access to projections of droplets onto the detector plane, estimates are made to determine the true average axes and aspect ratios. It is found that, although the superfluid droplets have a much higher average angular momentum, the two kinds of droplets have very similar average aspect ratios and, thus, similar average reduced angular momenta and reduced angular velocities. This observation may result from the formation of the droplets through turbulent nozzle flow and the atomization regime in the immediate vicinity of the nozzle. We conjecture that the droplets' rotation is driven by a combination of the liquid flow velocity gradient inside the nozzle and collisions close to it, leading to elongation and,

ultimately, fragmentation into daughter droplets, which may undergo repeated collisionelongation-fragmentation cycles.

Future studies will shed more light on the origin of angular momentum in droplets produced via fluid fragmentation. A large number of studies discuss the fragmentation of classical liquids upon jet expansion [55,56]. However, to the best of our knowledge, the amount of angular momentum contained in the resulting droplets remains unknown. It is therefore interesting to see that the jet atomization of classical liquids produces highly rotating droplets similar to quantum He droplets.

The availability of the large ³He droplets suitable for single-pulse diffraction experiments also opens additional research directions. Vortex-induced cluster aggregation has so far been unique to superfluid ⁴He. It is of high interest to expand diffraction experiments to non-superfluid ³He and study the aggregation patterns in rotating fermionic droplets. Dopant aggregation mechanisms and the morphology of the phase separation in rotating mixed ³He/⁴He droplets presents another frontier [57].

6. Acknowledgements

This material is based upon work supported by the National Science Foundation under Grant No. DMR-1701077 (A.F.V.). C.S., B.W.T., M.B. and O.G. are supported by the U.S. Department of Energy, Office of Science, Office of Basic Energy Sciences, Chemical Sciences, Geosciences and Biosciences Division, through Contract No. DE-AC02-05CH11231. M.B. acknowledges support by the Alexander von Humboldt foundation. Portions of this research were carried out at the Linac Coherent Light Source (LCLS) at the SLAC National Accelerator Laboratory, a user facility operated by Stanford University on behalf of the U.S. DOE, OBES under beam-time Grant No. LU46: Molecular Self-Assembly Close to 0 Kelvin. Use of LCLS is supported by the U.S. Department of Energy, Office of Science, Office of Basic Energy Sciences under Contract No. DE-AC02-76SF00515. We thank Manuel Barranco for carefully reading the manuscript and making Ref. [33] available to us prior to publication.

7. References

- [1] J. P. Toennies and A. F. Vilesov, Superfluid helium droplets: A uniquely cold nanomatrix for molecules and molecular complexes, Angewandte Chemie-International Edition 43, 2622 (2004).
- [2] M. Y. Choi, G. E. Douberly, T. M. Falconer, W. K. Lewis, C. M. Lindsay, J. M. Merritt, P. L. Stiles, and R. E. Miller, *Infrared spectroscopy of helium nanodroplets: Novel methods for physics and chemistry*, International Reviews in Physical Chemistry **25**, 15 (2006).
- [3] M. Barranco, R. Guardiola, S. Hernandez, R. Mayol, J. Navarro, and M. Pi, *Helium nanodroplets: An overview,* Journal of Low Temperature Physics **142**, 1 (2006).
- [4] R. M. P. Tanyag, C. F. Jones, C. Bernando, S. M. O. O'Connell, D. Verma, and A. F. Vilesov, in *Cold Chemistry: Molecular Scattering and Reactivity Near Absolute Zero*, edited by O. Dulieu, and A. Osterwalder (Royal Society of Chemistry, Cambridge, 2017), p. 389.
- [5] D. Verma, R. M. P. Tanyag, S. M. O. O'Connell, and A. F. Vilesov, *Infrared spectroscopy in superfluid helium droplets*, Advances in Physics-X **4**, 1553569 (2018).
- [6] A. Mauracher, O. Echt, A. M. Ellis, S. Yang, D. K. Bohme, J. Postler, A. Kaiser, S. Denifl, and P. Scheier, *Cold physics and chemistry: Collisions, ionization and reactions inside helium nanodroplets close to zero K*, Physics Reports-Review Section of Physics Letters **751**, 1 (2018).
- [7] S. Grebenev, J. P. Toennies, and A. F. Vilesov, *Superfluidity within a small helium-4 cluster: The microscopic Andronikashvili experiment*, Science **279**, 2083 (1998).
- [8] A. R. W. McKellar, Y. J. Xu, and W. Jager, *Spectroscopic exploration of atomic scale superfluidity in doped helium nanoclusters*, Physical Review Letters **97**, 183401 (2006).
- [9] M. Lemeshko and R. Schmidt, in *Cold Chemistry: Molecular Scattering and Reactivity Near Absolute Zero*, edited by O. Dulieu, and A. Osterwalder (Royal Society of Chemistry, Cambridge, 2017), p. 444.
- [10] L. F. Gomez, E. Loginov, R. Sliter, and A. F. Vilesov, *Sizes of large He droplets*, Journal of Chemical Physics **135**, 154201 (2011).
- [11] L. F. Gomez, K. R. Ferguson, J. P. Cryan, C. Bacellar, R. M. P. Tanyag, C. Jones, S. Schorb, D. Anielski, A. Belkacem, C. Bernando, R. Boll, J. Bozek, S. Carron, G. Chen, T. Delmas, L. Englert, S. W. Epp, B. Erk, L. Foucar, R. Hartmann, A. Hexemer, M. Huth, J. Kwok, S. R. Leone, J. H. S. Ma, F. R. N. C. Maia, E. Malmerberg, S. Marchesini, D. M. Neumark, B. Poon, J. Prell, D. Rolles, B. Rudek, A. Rudenko, M. Seifrid, K. R. Siefermann, F. P. Sturm, M. Swiggers, J. Ullrich, F. Weise, P. Zwart, C. Bostedt, O. Gessner, and A. F. Vilesov, *Shapes and vorticities of superfluid helium nanodroplets*, Science **345**, 906 (2014).
- [12] R. M. P. Tanyag, C. Bernando, C. F. Jones, C. Bacellar, K. R. Ferguson, D. Anielski, R. Boll, S. Carron, J. P. Cryan, L. Englert, S. W. Epp, B. Erk, L. Foucar, L. F. Gomez, R. Hartmann, D. M. Neumark, D. Rolles, B. Rudek, A. Rudenko, K. R. Siefermann, J. Ullrich, F. Weise, C. Bostedt, O. Gessner, and A. F. Vilesov, *Communication: X-ray coherent diffractive imaging by immersion in nanodroplets*, Structural Dynamics **2**, 051102 (2015).
- [13] C. F. Jones, C. Bernando, R. M. P. Tanyag, C. Bacellar, K. R. Ferguson, L. F. Gomez, D. Anielski, A. Belkacem, R. Boll, J. Bozek, S. Carron, J. Cryan, L. Englert, S. W. Epp, B. Erk, L. Foucar, R. Hartmann, D. M. Neumark, D. Rolles, A. Rudenko, K. R. Siefermann, F. Weise, B. Rudek, F. P. Sturm, J. Ullrich, C. Bostedt, O. Gessner, and A. F. Vilesov, *Coupled motion of Xe clusters and quantum vortices in He nanodroplets*, Physical Review B **93**, 180510(R) (2016).
- [14] C. Bernando, R. M. P. Tanyag, C. Jones, C. Bacellar, M. Bucher, K. R. Ferguson, D. Rupp, M. P. Ziemkiewicz, L. F. Gomez, A. S. Chatterley, T. Gorkhover, M. Muller, J. Bozek, S. Carron,

- J. Kwok, S. L. Butler, T. Moller, C. Bostedt, O. Gessner, and A. F. Vilesov, *Shapes of rotating superfluid helium nanodroplets*, Physical Review B **95**, 064510 (2017).
- [15] D. Rupp, N. Monserud, B. Langbehn, M. Sauppe, J. Zimmermann, Y. Ovcharenko, T. Moller, F. Frassetto, L. Poletto, A. Trabattoni, F. Calegari, M. Nisoli, K. Sander, C. Peltz, M. J. Vrakking, T. Fennel, and A. Rouzee, *Coherent diffractive imaging of single helium nanodroplets with a high harmonic generation source*, Nature Communications **8**, 493 (2017).
- [16] B. Langbehn, K. Sander, Y. Ovcharenko, C. Peltz, A. Clark, M. Coreno, R. Cucini, M. Drabbels, P. Finetti, M. Di Fraia, L. Giannessi, C. Grazioli, D. Iablonskyi, A. C. LaForge, T. Nishiyama, V. O. A. de Lara, P. Piseri, O. Plekan, K. Ueda, J. Zimmermann, K. C. Prince, F. Stienkemeier, C. Callegari, T. Fennel, D. Rupp, and T. Moller, *Three-dimensional shapes of spinning helium nanodroplets*, Physical Review Letters 121, 255301 (2018).
- [17] S. M. O. O'Connell, R. M. P. Tanyag, D. Verma, C. Bernando, W. Pang, C. Bacellar, C. A. Saladrigas, J. Mahl, B. W. Toulson, W. Kumagai, P. Walter, F. Ancilotto, M. Barranco, M. Pi, C. Bostedt, O. Gessner, and A. F. Vilesov, *Angular momentum in rotating superfluid droplets*, Physical Review Letters **in press** (2020).
- [18] K. Lehman and R. Schmied, *Energetics and possible formation and decay mechanisms of vortices in helium nanodroplets*, Physical Review B **68**, 224520 (2003).
- [19] O. Gessner and A. Vilesov, *Imaging Quantum Vortices in Superfluid Helium Droplets*, Annual Review of Physical Chemistry **70**, 173 (2019).
- [20] F. Ancilotto, M. Barranco, and M. Pi, *Spinning superfluid He-4 nanodroplets*, Physical Review B **97**, 184515 (2018).
- [21] F. Ancilotto, M. Pi, and M. Barranco, *Vortex arrays in nanoscopic superfluid helium droplets*, Physical Review B **91**, 100503 (2015).
- [22] J. Gspann and H. Vollmar, *Metastable Excitations of Large Clusters of ³He*, ⁴He or Ne Atoms, Journal of Chemical Physics **73**, 1657 (1980).
- [23] P. W. Stephens and J. G. King, *Experimental investigation of small helium clusters Magic numbers and the onset of condensation*, Physical Review Letters **51**, 1538 (1983).
- [24] K. vonHaeften, A. R. B. deCastro, M. Joppien, L. Moussavizadeh, R. vonPietrowski, and T. Moller, *Discrete visible luminescence of helium atoms and molecules desorbing from helium clusters: The role of electronic, vibrational, and rotational energy transfer,* Physical Review Letters **78**, 4371 (1997).
- [25] M. Farnik, U. Henne, B. Samelin, and J. P. Toennies, *Differences in the detachment of electron bubbles from superfluid* ⁴He droplets versus nonsuperfluid ³He droplets, Physical Review Letters **81**, 3892 (1998).
- [26] J. Harms, M. Hartmann, B. Sartakov, J. P. Toennies, and A. F. Vilesov, *High resolution infrared spectroscopy of single SF*₆ molecules in helium droplets. II. The effect of small amounts of ⁴He in large ³He droplets, Journal of Chemical Physics **110**, 5124 (1999).
- [27] J. Harms, J. P. Toennies, M. Barranco, and M. Pi, Experimental and theoretical study of the radial density distributions of large ³He droplets, Physical Review B **63**, 184513 (2001).
- [28] F. Stienkemeier, O. Bunermann, R. Mayol, F. Ancilotto, M. Barranco, and M. Pi, *Surface location of sodium atoms attached to ³He nanodroplets*, Physical Review B **70**, 214509 (2004).
- [29] B. G. Sartakov, J. P. Toennies, and A. F. Vilesov, *Infrared spectroscopy of carbonyl sulfide inside a pure* ³*He droplet*, Journal of Chemical Physics **136**, 134316 (2012).
- [30] S. Grebenev, B. G. Sartakov, J. P. Toennies, and A. F. Vilesov, *The structure of the OCS-H₂ van der Waals complex embedded inside* ${}^{4}He/{}^{3}He$ *droplets*, Journal of Chemical Physics **114**, 617 (2001).

- [31] D. R. Tilley and J. Tilley, *Superfluidity and superconductivity* (Institute of Physics Publishing, Bristol, 1990).
- [32] E. R. Dobbs, *Helium Three* (Oxford University Press, New York, 2000).
- [33] M. Pi, F. Ancilotto, and M. Barranco, *Rotating ³He droplets*, Journal of Chemical Physics **152**, 184111 (2020).
- [34] R. A. Brown and L. E. Scriven, *The shape and stability of rotating liquid-drops*, Proceedings of the Royal Society of London Series a-Mathematical Physical and Engineering Sciences **371**, 331 (1980).
- [35] S. L. Butler, M. R. Stauffer, G. Sinha, A. Lilly, and R. J. Spiteri, *The shape distribution of splash-form tektites predicted by numerical simulations of rotating fluid drops*, Journal of Fluid Mechanics **667**, 358 (2011).
- [36] See Supplementary Materials for more information on ³He/⁴He P-T diagrams, detection probability of He droplets, list of experimental runs, and the ³He recycling system.
- [37] D. M. Brink and S. Stringari, *Density of States and Evaporation Rate of Helium Clusters*, Zeitschrift Fur Physik D **15**, 257 (1990).
- [38] R. D. Mc Carty, Journal of Physical and Chemical Reference Data 2, 923 (1973).
- [39] R. M. Gibbons and D. I. Nathan, *Thermodyanamic data of helium-3*, Technical Report AFML-TR-67-175 (1967).
- [40] B. Samelin, PhD thesis, *Lebensdauer und neutralisation metastabiler, negative geladener Helium-Mikrotropfen*, University of Göttingen (1998).
- [41] M. Hartmann, Ph.D. Thesis, *Hochauflösende Spekrtoskopie von Molekülen in 4-Helium-und 3-Helium-Clustern*, University of Göttingen (1997).
- [42] F. Pobell, Matter and methods at low temperatures (Springer, Berlin, 2007).
- [43] L. Struder, S. Eppa, D. Rolles, R. Hartmann, P. Holl, G. Lutz, H. Soltau, R. Eckart, C. Reich, K. Heinzinger, C. Thamm, A. Rudenko, F. Krasniqi, K. U. Kuhnel, C. Bauer, C. D. Schroter, R. Moshammer, S. Techert, D. Miessner, M. Porro, O. Halker, N. Meidinger, N. Kimmel, R. Andritschke, F. Schopper, G. Weidenspointner, A. Ziegler, D. Pietschner, S. Herrmann, U. Pietsch, A. Walenta, W. Leitenberger, C. Bostedt, T. Moller, D. Rupp, M. Adolph, H. Graafsma, H. Hirsemann, K. Gartner, R. Richter, L. Foucar, R. L. Shoeman, I. Schlichting, and J. Ullrich, Large-format, high-speed, X-ray pnCCDs combined with electron and ion imaging spectrometers in a multipurpose chamber for experiments at 4th generation light sources, Nuclear Instruments & Methods in Physics Research Section a-Accelerators Spectrometers Detectors and Associated Equipment 614, 483 (2010).
- [44] K. R. Ferguson, M. Bucher, J. D. Bozek, S. Carron, J. C. Castagna, R. Coffee, G. I. Curiel, M. Holmes, J. Krzywinski, M. Messerschmidt, M. Minitti, A. Mitra, S. Moeller, P. Noonan, T. Osipov, S. Schorb, M. Swiggers, A. Wallace, J. Yin, and C. Bostedt, *The atomic, molecular and optical science instrument at the linac coherent light source*, Journal of Synchrotron Radiation 22, 492 (2015).
- [45] M. P. Kühnel, N.; Winters, D. F. A.; Popp, U.; Dörner, R.; Stöhlker, T.; Grisenti, R. E., Low-Z internal target from a cryogenically cooled liquid microjet source, Nuclear Instruments & Methods in Physics Research **602**, 311 (2009).
- [46] R. M. P. Tanyag, A. J. Feinberg, S. M. O. O'Connell, and A. F. Vilesov, *Disintegration of diminutive liquid helium jets in vacuum*, Journal of Chemical Physics **in press** (2020).
- [47] R. M. P. Tanyag, PhD thesis, *Imaging superfluid helium droplets*, University of Southern California (2018).

- [48] U. Henne and J. P. Toennies, *Electron capture by large helium droplets*, Journal of Chemical Physics **108**, 9372 (1998).
- [49] R. J. Donnelly and C. F. Barenghi, *The observed properties of liquid helium at the saturated vapor pressure*, Journal of Physical and Chemical Reference Data **27**, 1217 (1998).
- [50] M. Iino, M. Suzuki, A. J. Ikushima, and Y. Okuda, *Surface tension of liquid ³He down to 0.3 K*, J. Low Temp. Phys. **59**, 291 (1985).
- [51] L. F. Gomez, E. Loginov, and A. F. Vilesov, *Traces of vortices in superfluid helium droplets*, Physical Review Letters **108**, 155302 (2012).
- [52] R. E. Grisenti and J. P. Toennies, *Cryogenic microjet source for orthotropic beams of ultralarge superfluid helium droplets*, Physical Review Letters **90**, 234501 (2003).
- [53] G. F. Bertsch, T. Kawano, and L. M. Robledo, *Angular momentum of fission fragments*, Physical Review C **99**, 034603 (2019).
- [54] L. Bonneau, P. Quentin, and I. N. Mikhailov, *Scission configurations and their implication in fission-fragment angular momenta*, Physical Review C **75**, 064313 (2007).
- [55] C. Dumouchel, On the experimental investigation on primary atomization of liquid streams, Experiments in Fluids 45, 371 (2008).
- [56] J. Eggers and E. Villermaux, *Physics of liquid jets*, Reports on Progress in Physics **71**, 036601 (2008).
- [57] M. Barranco, M. Guilleumas, D. M. Jezek, R. J. Lombard, J. Navarro, and M. Pi, *Nucleation in dilute* ³*He-*⁴*He liquid mixtures at low temperatures*, Journal of Low Temperature Physics **117**, 81 (1999).